JGR Planets

RESEARCH ARTICLE
10.1029/2021JE006937

Yang Zhao and Lei Zhong contributed equally to this work and share joint first authorship.

Key Points:

- High dust loading decelerates the recession of southern CO_2 ice cap, while the extent of northern CO_2 ice cap is hardly affected by dust
- When Martian dust storm starts early, the appearance of the warming vortex is delayed and its intensity weakens
- The increase in northern surface CO_2 ice is induced by the increased polar-equator temperature gradient and the increased meridional flow

Supporting Information:

Supporting Information may be found in the online version of this article.

Correspondence to:

L. Zhong,
zhonglei@ustc.edu.cn

Citation:

Zhao, Y., Zhong, L., Yuan, R., Zhao, C., Li, R., Wang, Y., et al. (2021). Simulation of Martian dust effects on polar CO_2 ice caps and atmospheric circulation using the MarsWRF model. *Journal of Geophysical Research: Planets*, *126*, e2021JE006937. https://doi.org/10.1029/2021JE006937

Received 30 APR 2021
Accepted 4 DEC 2021

© 2021. American Geophysical Union. All Rights Reserved.

Simulation of Martian Dust Effects on Polar CO_2 Ice Caps and Atmospheric Circulation Using the MarsWRF Model

Yang Zhao[1], Lei Zhong[1,2,3], Renming Yuan[1,3], Chun Zhao[1,2,3], Rui Li[1,2,3], Yu Wang[1,2,3], Yuan Lian[4], and Mark Richardson[4]

[1]School of Earth and Space Sciences, University of Science and Technology of China, Hefei, China, [2]CAS Center for Excellence in Comparative Planetology, Hefei, China, [3]Frontiers Science Center for Planetary Exploration and Emerging Technologies, University of Science and Technology of China, Hefei, China, [4]Aeolis Research, Chandler, AZ, USA

Abstract Martian dust plays an important role in modulating climate. However, the effects of dust on polar CO_2 ice caps, atmospheric circulation processes and the relationship between them are not yet clear. In this study, a Mars general circulation model (MarsWRF) was applied to investigate the impacts of the magnitude and timing of Martian dust storms on the spatiotemporal characteristics of polar CO_2 ice caps and atmospheric circulation. The results show that dust can inhibit the sublimation of southern CO_2 ice through the radiation effect. Under the “High Dust” scenario, the ice edge can extend up to 5° more equatorward than that under the “Standard” scenario around Ls = 220°. The extent of northern CO_2 ice cap is hardly affected by dust because the impacts induced by dust mainly appear north of 80°N. By shifting the timing of maximum dust loading during the dust season, the "Early Dust" scenario inhibits the sublimation of the southern ice cap, while the "Late Dust" scenario accelerates the sublimation process. In addition, the variations in dust loading strength can lead to changes in three near-surface wind belts, which are related to intensified Hardly circulation. The appearance of the warming vortex under the "Early Dust" scenario is delayed, and its intensity is 60 K lower than that observed in the "High Dust" and "Late Dust" scenarios. When dust loading increases, the northern CO_2 condensation process in the Western Hemisphere accelerates, which is due to the increased pole-to-equator temperature gradient and the increased meridional wind speed.

Plain Language Summary Dust has a strong influence on the Martian climate. However, the dust effects on polar CO_2 ice caps and wind fields have not yet been fully investigated. In this study, a numerical model that simulates the Martian climate was applied to investigate changes in the spatial and temporal patterns of CO_2 ice caps and three-dimensional wind fields. The results show that dust can inhibit the sublimation of southern CO_2 ice by influencing the surface energy balance, while the coverage area of the northern CO_2 ice cap is hardly affected by dust because the impacts induced by dust mainly appear north of 80°N. In terms of the timing of Martian dust storms, when a dust storm starts early (late), the sublimation of the southern ice cap is inhibited (accelerated). The appearance of the warming vortex will be delayed and its temperature will be 60 K lower than that in the general scenario if the dust storm starts early. When dust loading increases, the northern surface CO_2 ice in the Western Hemisphere also increases, which is due to the increased pole-to-equator temperature gradient and increased meridional wind speed.

1. Introduction

As common dynamic processes, Martian dust activities are the major radiative processes that affect the global energy budget. The dust in the Martian atmosphere can absorb and scatter visible and thermal infrared radiation, therefore, playing an important role in modulating the climate (Rafkin et al., 2013). Affected by the eccentricity of the Martian orbit, the dust amounts lifted by dust devils in the Southern Hemisphere, which are thermally driven vortices in the atmosphere, are one order of magnitude greater than those in the Northern Hemisphere (Whelley & Greeley, 2008). Many studies have investigated the climatic effects induced by dust on Mars. For example, Towner (2009) found that the surface shadowed by airborne dust is colder than the surrounding areas due to the decrease in solar radiation by analyzing Mars Odyssey Thermal Emission Imaging System images. Kass et al. (2019) studied the air temperature characteristics during the growth, mature, and decay phases of the global dust storm in 2018, and found the air temperature increase to be very rapid in the mature phase. In addition, it is worth noting that a transient northern winter polar vortex warming event appears when a planetary-scale dust storm occurs, and the polar temperature and the nature of the polar vortex change accordingly (Forget et al., 1999;

Guzewich et al., 2016; Kuroda et al., 2009). Some studies have proven that this warming phenomenon is a response to the development of a pole-to-pole solstitial Hadley circulation and the doubling of the mass flux of the meridional circulation resulting from greatly increased dust loading (Guzewich et al., 2016; Haberle et al., 1993; Wilson, 1997).

Previous studies on the impacts of dust on the Martian climate have always focused on changes in the temporal-spatial distribution or vertical structure of temperature. For CO_2, the main component of the Martian atmosphere, its sublimation and condensation flows are also closely related to the energy stored in the surface and atmosphere (Chow et al., 2019; Piqueux et al., 2015). Therefore, the changes in Martian energy distribution induced by dust may influence the phase transition process of polar ice caps, which has rarely been considered in previous studies. The surface CO_2 ice caps in MY25 with a global dust storm are compared with that in MY26 with no global dust storm by analyzing the Mars Analysis Correction Data Assimilation (MACDA v1.0) (Figure S1 in Supporting Information S1). It is found that during the dust storm, the southern CO_2 ice in MY25 is more extensive than that in MY26, while the northern CO_2 ice is less than that in MY26. These phenomena indicate that Martian dust may inhibit the southern CO_2 ice sublimation process and northern CO_2 condensation process. In general, dust may influence the phase transition process of polar CO_2 ice caps in two ways: the direct radiation effect, that is, scattering solar radiation and emitting long-wave radiation, and the redistribution of temperature by changing atmospheric circulation. Both of these factors are taken into account when studying the effects of dust on Martian CO_2 in this study. In addition to the interannual difference in the magnitude of dust loading, the timing of dust storms in different years also varies. For example, the dust storm in MY25 occurred at Ls = 190–250° (Ls is the areocentric solar longitude), and the dust storm in MY28 appeared at Ls = 270–300°. However, there has been no investigation thus far on the impact of dust loading timing on the CO_2 ice cap and atmospheric circulation.

Various Martian atmospheric models have been developed to compensate for the limited temporal-spatial resolution of observation data. MarsWRF has been one of the most used models for researching the Martian atmosphere in recent years (Richardson et al., 2007). MarsWRF can properly reproduce the temporal and spatial variation characteristics of variables for Mars, such as CO_2 ice, wind field, and radiation flux levels (Banfield et al., 2020; Chow et al., 2019; Fonseca et al., 2018; Newman, Kahanpää, et al., 2019). In addition, the model is capable of simulating the interannual variations in the dust mixing ratio and dust particle sizes (Senel et al., 2021), and can be used to forecast dust storms (Newman, Lee, et al., 2019) and provide microscale simulations in a fully interactive mode (Wu et al., 2021). To study the effect of the strength and timing of dust storms on Martian CO_2 ice cap and atmospheric circulation, five sensitivity experiments were performed with MarsWRF by modifying the default dust distribution scheme in this study. The structure of the paper is as follows. The model configuration and case designs are introduced in Section 2. Section 3 establishes a baseline comparison between the observations and model predictions, and then investigates the impacts of the magnitude and timing of Martian dust storm on polar CO_2 ice caps and atmospheric circulation. Finally, conclusions are presented in Section 4.

2. The Numerical Model

The MarsWRF general circulation model (GCM) (Richardson et al., 2007; Toigo et al., 2012) is used in this study to examine the impacts induced by dust. MarsWRF is the Mars version of the PlanetWRF model. In this study, the radiative feedbacks of dust aerosols are parameterized in the correlated-k coefficient model (KDM) (Mischna et al., 2012; Newman & Richardson, 2015), which includes 14 solar and infrared bands for dust. MarsWRF can be configured to use a variety of dust parameterizations. This study chose a prescribed dust scenario, an analytic fit to the dust optical depth obtained from the Mars Climate Database (MCD) "MGS dust scenario" (Montabone et al., 2014; Montmessin et al., 2004; Toigo et al., 2012), to study the impacts of the strength and timing of dust loading on the Martian atmosphere. To perform a mechanistic study, the "MCD-MGS" dust scenario was chosen due to its simplicity and highly controllable spatial and temporal profiles. We consider the dust lifting by both the near-surface wind stress and dust devil, where the threshold value for local near-surface stress is set to 0.043 N/m^2 according to Xiao et al. (2019). The rate parameters for near-surface wind stress lifting and dust devil lifting are set to 8.5×10^{-5} and 1.0×10^{-9}, respectively, according to Gebhardt et al. (2021). With this set of values, MarsWRF can effectively present the characteristics of dust lifting activities. The lifted dust is only designed for demonstration purpose, it is not radiatively interactive. The type of dust microphysics determines the dust size distribution, such as single dust particle size, two particle sizes, and two moment dust. Different dust size

Table 1
WRF Configurations

Physical processes	Parameterization schemes
Boundary layer	Medium Range Forecast Model (MRF) (Hong & Pan, 1996)
Microphysics	Marsdust1size
Longwave radiation	Correlated-k coefficient model (KDM) (Mischna et al., 2012)
Shortwave radiation	Correlated-k coefficient model (KDM) (Mischna et al., 2012)
Surface layer	Monin-Obukhov scheme (Jiménez et al., 2012)
Land surface	Martian 12-layer subsurface diffusion scheme
Dust distribution	Mars Climate Database (MCD) “MGS dust scenario” (Montmessin et al., 2004)

distributions can impact the sedimentation processes. In this study, the single-sized dust particle (marsdust1size) scheme was chosen during sedimentation processes. The other parameterization schemes are shown in Table 1.

The comparison between the prescribed dust optical depth and the 8-year averaged distribution of dust optical depth from the reconstructed observational data shows that the MCD-MGS dust scenario (Figure 1b) is able to capture the major characteristics of the Martian dust distribution (Figure 1a), particularly the significant increase in global dust opacity after Ls = 180°. Both the observation and simulation show that dust is mainly distributed in the Southern Hemisphere, and its lifting activities are strong in L_S = 220°–280°. However, there is some discrepancy between the prescribed and observational data. For instance, the prescribed dust shows a higher dust optical depth overall and it does not capture the episode of increased dust occurring near Ls = 320°.

Here, we experiment with five cases designated as “Low Dust,” “Standard,” “High Dust,” “Early Dust,” and “Late Dust” (Figure 1c). The “Standard” case represents the default dust distribution in the MGS dust scenario. The “Low Dust” (“High Dust”) case halve (double) the peak optical depth under the “Standard” scenario to investigate the effects of dust loading. In order to study the effects of the timing of dust storm, the timing of peak dust loading is changed from Ls = 250° for the “High Dust” scenario to Ls = 230° and Ls = 280° for the “Early Dust” and “Late Dust” cases, respectively. All simulations are run with a 5° horizontal grid resolution (equivalent to 36 × 72 latitude and longitude grid points). There are 52 vertical levels in the terrain-following hybrid sigma vertical coordinates (Skamarock & Klemp, 2008). The model top is limited to 80 km. We run each aforementioned case for two Martian years, with the first year being the spin-up period.

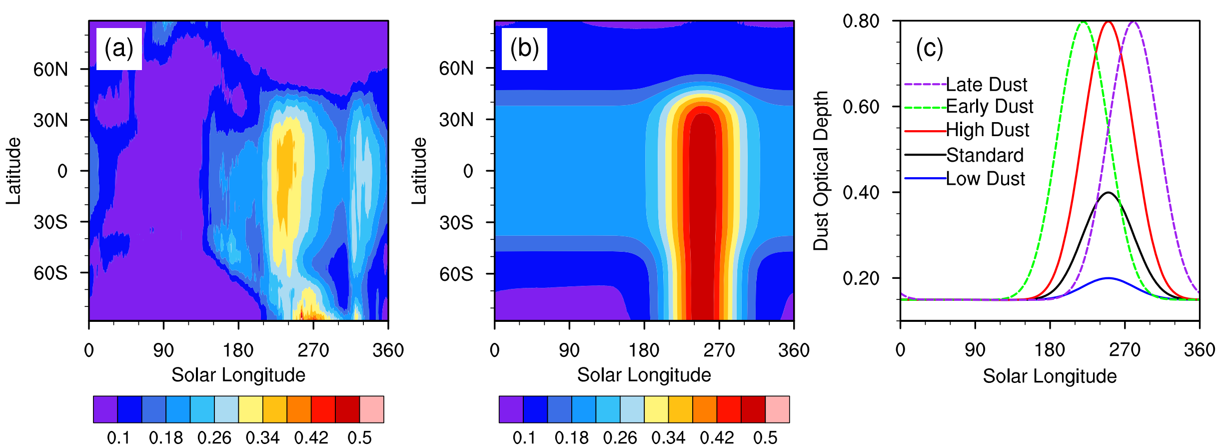

Figure 1. (a) The reconstructed observational dust optical depth (Montabone et al., 2015) averaged for Martian years (MY) 24–33 excluding MY 25 and 28 because the two years includes global-scale dust storms. (b) Latitudinal and seasonal variation in column dust optical depth (normalized to 700 Pa) for the "Standard" dust scenarios. (c) Annual variation curves of dust optical depth in different cases. The black line denotes the "Standard" scenario (the peak value is 0.4 at Ls = 250°), the red line denotes the “High Dust” scenario (twice the peak dust opacity), the blue line denotes the “Low Dust” scenario (half the peak dust opacity), the green line denotes the "Early Dust" scenario (the peak occurs at Ls = 230°), and the purple line is the "Late Dust" scenario (the peak occurs at Ls = 280°).

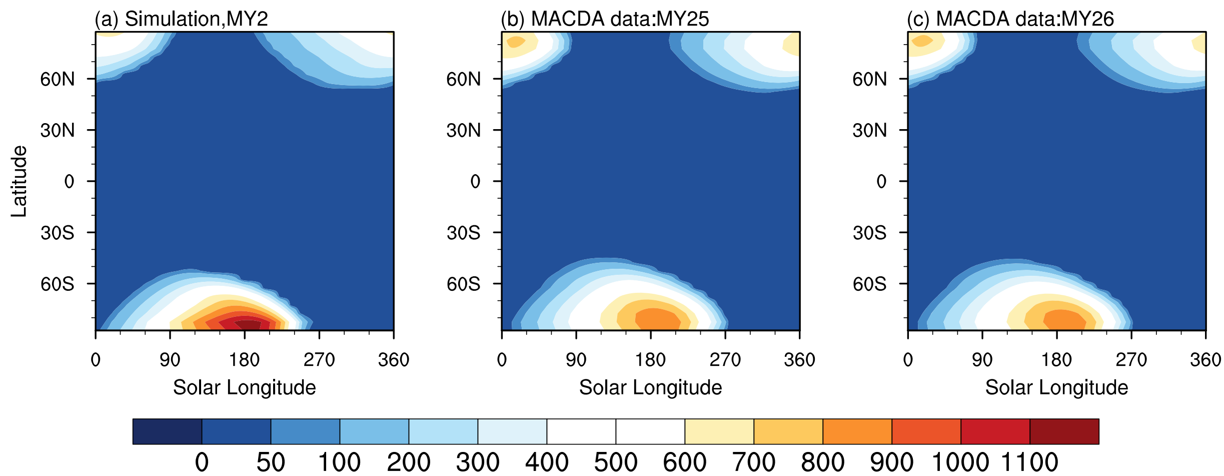

Figure 2. Latitude-time variation in zonal-mean carbon dioxide ice (kg/m^2) from the (a) "Standard" scenario, (b) MY25 of MACDA v1.0, and (c) MY26 of MACDA v1.0.

3. Results

3.1. Baseline Comparison

To evaluate the performance of the modeling system, the simulation results of the "Standard" scenario, a case closest to the usual conditions, were compared with the observed annual variation in zonal-mean CO_2 ice (Figure 2). The simulation results show that the "Standard" case can reproduce the evolution pattern of the CO_2 ice cap obtained from MACDA v1.0, which is publicly available from the Centre for Environmental Data Analysis (Montabone et al., 2014). However, compared to the observations, the model overpredicts and underpredicts the surface CO_2 ice in the Southern and Northern Hemispheres, respectively. This comparison is qualitative because there may be some uncertainties in the distribution of CO_2 ice in the reanalyzed data, which have not yet been fully validated by observations (Chow et al., 2018).

The study used the extensive temporal-spatial coverage provided by the Mars Climate Probe (MCS) onboard the Mars Reconnaissance Orbiter (MRO) to assess the simulated air temperature. The MCS is an infrared radiometer observed in eight thermal infrared channels using limb and on-planet viewing (McCleese et al., 2007). The instrument observes in a polar, sun-synchronous orbit that yields observations nominally centered at 0300 and 1500 local solar time (LT). Temperature and aerosol retrievals produce measurements from the surface to ~80 km in altitude (Kleinböhl et al., 2009, 2011). Figure 3 shows the MCS latitude-pressure profiles of zonal mean temperature around the northern winter solstice in MY 28–31. In MY 28, where a global-scale dust storm occurred (Figure 3a), the air temperature over the northern polar region below 0.1 Pa is higher than that in other years (Figures 3b–3d), while the atmospheric temperature over the tropical region decreased. These phenomena are consistent with the temperature characteristics under the simulated "High Dust" scenario (Figure 4c). The simulated temperature in the "Standard" scenario (Figure 4b) is also in good agreement with that in the quiescent years (Figures 3b–3d); that is, the temperature contours exhibit similar latitudinal structures with comparable magnitude in both hemispheres.

To evaluate whether MarsWRF is able to reproduce the observed near-surface wind variations, we compare the wind direction and wind speed measured by Insight Lander with the simulated values (Figure 5). InSight landed at 4.5°N 135.9°E on 26 November 2018. Data currently available covers the period from 2018-11-30 to 2020-10-14 (Ls 298 MY 34 to Ls 295.0 MY 35). The Temperatures and Wind Sensor for Insight (TWINS) instrument, which is used to measure near-surface temperature and wind fields, is comprised of two identical booms that are placed on opposite sides of the lander deck, one pointing in the -Y lander axis direction (BMY) and the other pointing in the +Y direction (BPY) (Banfield et al., 2019, 2020; Spiga et al., 2018). The booms are positioned ~1.2 m above ground level. At the landing site, the observed wind direction is about 200° for the BMY measurement (south-westerly) and about 140° for the BPY measurement (south-easterly) during the first half of the Martian year and fluctuates at ~270° (westerly) during the second half of the Martian year (Figures 5a and 5c). For the simulated wind fields (averaged over 2.5–7.5°N, 132.5–137.5°E), the wind direction is maintained at

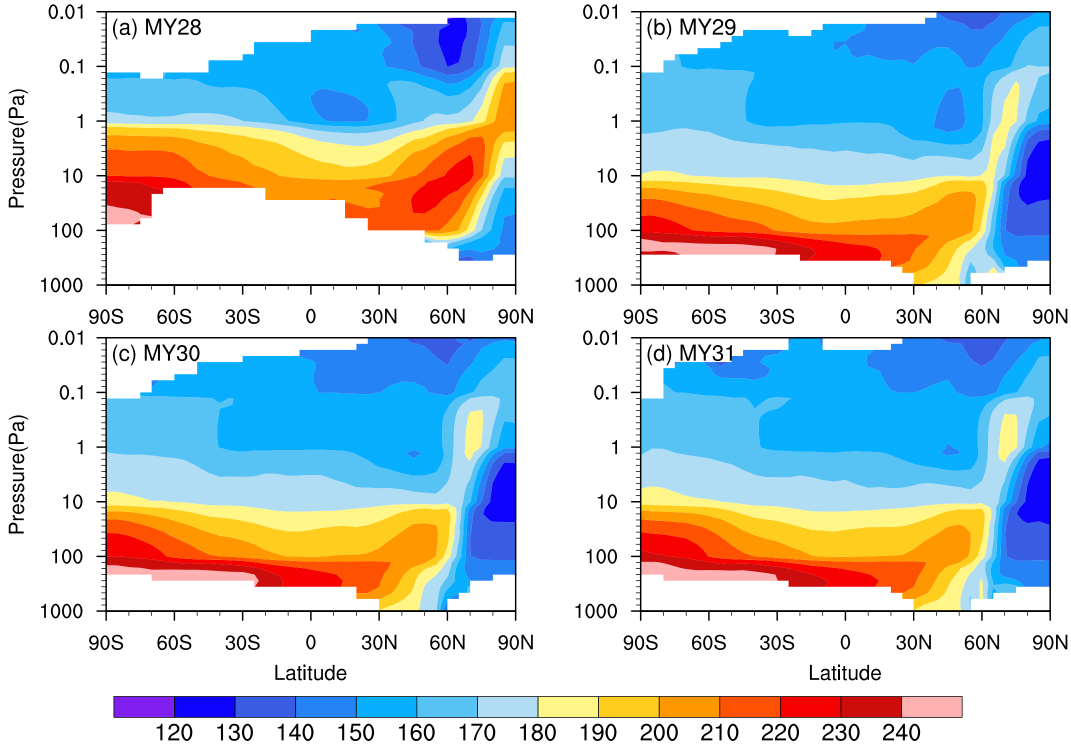

Figure 3. Mars Climate Probe zonal mean temperatures (K) for Ls = 267.8–272.3° (around the northern winter solstice) in (a) MY 28, (b) MY 29, (c) MY 30, and (d) MY 31.

~140° (south-easterly) in the first half of the Martian year and fluctuates between 340–360° (0°) (north-westerly) in the second half of the Martian year (Figures 5a and 5c). Regarding the wind speed, although the values measured by BMY and BPY are not completely consistent, both show an obvious decrease during the period of Ls = 160–200°, which is also demonstrated in the simulation results (Figures 5b and 5d). The above analysis indicates that the simulation results for the wind fields from the MarsWRF model are reliable.

3.2. Impact of Dust Loading Strength on CO_2 Ice Caps

CO_2 ice on Mars is mainly distributed throughout high latitudes of the Northern and Southern Hemispheres and it sublimates or condenses with seasonal changes. To explore the possible impacts of dust loading on the temporal and spatial distribution of CO_2 ice, we analyze the surface radiation fluxes during the period when southern CO_2 ice is in the sublimation state. We assume that the distribution of the surface CO_2 ice is zonally symmetric (Figures S2 and S3 in Supporting Information S1) and chose the data at 2.5 W-2.5 E where the local true solar time corresponds to the universal time to analyze. The annual variation of the CO_2 ice coverage is also considered. For example, the southern CO_2 ice is mainly distributed south of 65°S at Ls = 210° (Figure S2 in Supporting Information S1) and south of 70°S at Ls = 230° (Figure S3 in Supporting Information S1). Therefore, the areas that are used to calculate the averages at different times are not same. Figure 6 shows that the temporal variation and magnitude of surface net radiation flux (net downward short-wave flux + downward long-wave flux—upward long-wave radiation emitted from the surface) and latent heat flux are in good agreement. This phenomenon indicates that the sublimation of CO_2 leads to latent cooling of the surface, which counteracts with the radiative heating of the surface. It is also found that both the surface net radiation flux and latent heat flux decrease with increasing dust loading because higher dust loading scatters more solar shortwave radiation before it reaches the surface; that is, dust can inhibit the sublimation of southern CO_2 ice through the radiation effect.

Southern surface CO_2 ice mass under various dust loading scenarios and its difference relative to the “Standard" scenario are given in Figures 7 and 8, respectively. Compared to the “Standard” dust scenario, the southern ice cap retreats faster over the time (Figures 7a–7d) and the surface ice mass is always smaller in the “Low Dust” scenario (Figures 8a–8d). Likewise, the recession of the southern ice cap is slower (Figures 7i–7l) and the surface

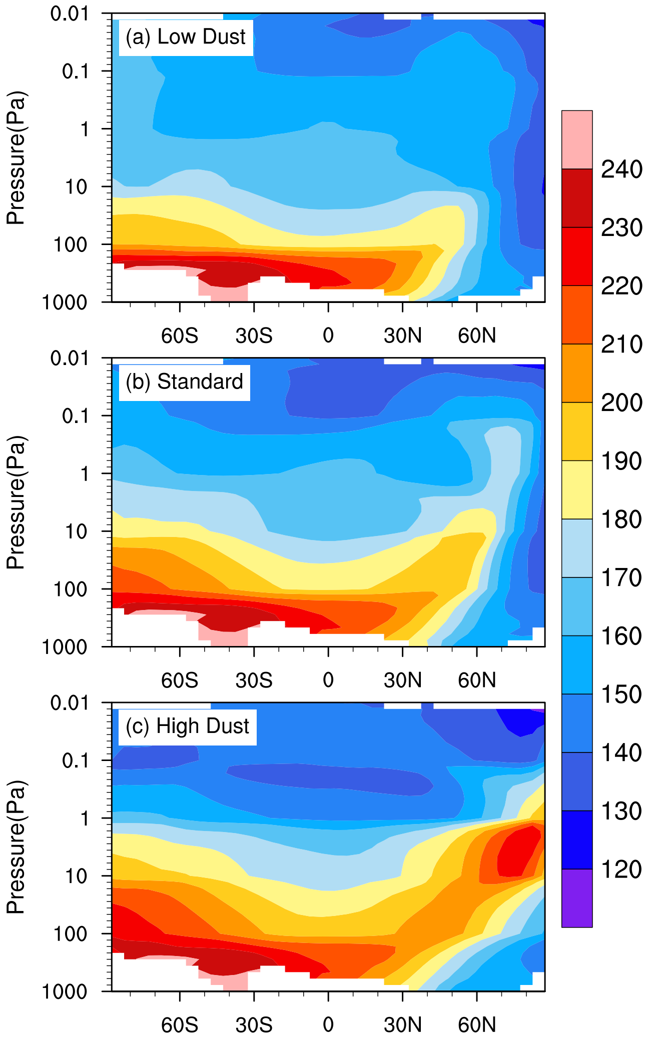

Figure 4. Simulated zonal mean temperatures (K) for Ls ≈ 270° (around the northern winter solstice) in the (a) "Low Dust," (b) "Standard," and (c) "High Dust" scenarios.

CO_2 ice mass is larger in the case of "High Dust" (Figures 8e–8h). At the onset of the sublimation process of southern ice cap (Ls = 200°), the effect of dust loading strength on the surface CO_2 ice is almost indiscernible. Around Ls = 220°, the "High (Low) Dust" scenario increases (decreases) the surface CO_2 ice mass by as much as 50 kg/m^2 compared with that in the "Standard" scenario. The difference further increases to about 100 kg/m^2 at ~Ls = 240° (Figure 8). The influence of dust on the southern ice cap edge mainly occurs between Ls = 200° and Ls = 240°. The location of the southern ice edge at Ls = 220° under the "High Dust" scenario can extend up to 5° more equatorward than that under the "Standard" scenario (Figures 7f and 7j).

Since 96% of the atmospheric composition on Mars is CO_2, the surface pressure is a physical quantity closely related to the phase state of the Martian CO_2 ice cap. The annual variations of surface pressure at the mid-to-high latitudes for both hemispheres are provided in Figure 9, which shows that higher dust loading generally results in lower surface pressure at the southern high latitudes (Figure 9a) between Ls = 200° and Ls = 360° because dust has an inhibitory effect on the sublimation of southern CO_2 ice. However, the surface pressure in the northern ice caps under the "High Dust" scenario increases suddenly during the period of Ls = 240–300° (Figure 9b), and the "transient vortex warming" event appears at the same time (Figure S4 in Supporting Information S1). The dichotomy between the southern and northern surface pressure is a result of increased atmospheric temperature in the Northern Hemisphere under the "High Dust" scenario, as higher dust loading reduces the condensation of CO_2 and results in more gaseous CO_2, higher surface pressure and less surface CO_2 ice mass in the northern polar region. However, there exists regions with increased surface CO_2 ice in 0–180W° (Figures S5e-S5h in Supporting Information S1). This phenomenon is related to changes in atmospheric circulation, which are explained in detail in Section 3.4. Examination of the hemispheric mean (Figures 9a and 9b) and the global mean (Figure 9c) of surface pressure suggests that the temporal changes of surface pressure in the Northern and Southern Hemispheres exhibit cancellation patterns relative to the global mean (note that the global mean surface pressure shows little difference under the three dust scenarios). In addition, unlike the southern ice cap changes, the coverage of the northern ice cap undergoes almost no change under different dust loading scenarios (Figure S6 in Supporting Information S1) because the impact of the warming vortex on the northern ice cap mainly appears in the north of 80°N (Figure S5 in Supporting Information S1).

3.3. Impact of Dust Loading Timing on CO_2 Ice Caps

In addition to the magnitude of dust loading, we also vary the timing of maximum dust loading during a Martian year as sensitivity studies. From an investigation of dust storms with different timings, it is found that the effects of dust storms in the "Early Dust" and "Late Dust" scenarios on southern CO_2 ice cap sublimation show opposite behaviors: the dust storm under the "Early Dust" scenario inhibits the sublimation of the southern ice cap (Figures 10a–10d), while the dust storm under the "Late Dust" scenario accelerates the sublimation process (Figures 10e–10h).

It is well-known that the influence of dust on the surface energy balance involves two processes: dust can absorb/scatter solar radiation and reduce the short-wave radiation flux reaching the ground; dust also emits long-wave radiation, increasing the energy reaching the ground surface. The differences in the downward short-wave flux (SWD) and downward long wave flux (LWD) at the ground between "Early Dust" and "Late Dust" scenarios and the "Standard" scenario are given in Figures S7 and S8 in Supporting Information S1, respectively. During the sublimation of southern CO_2 ice (before Ls = 270°), the SWD in "Early Dust" scenario can decrease by as

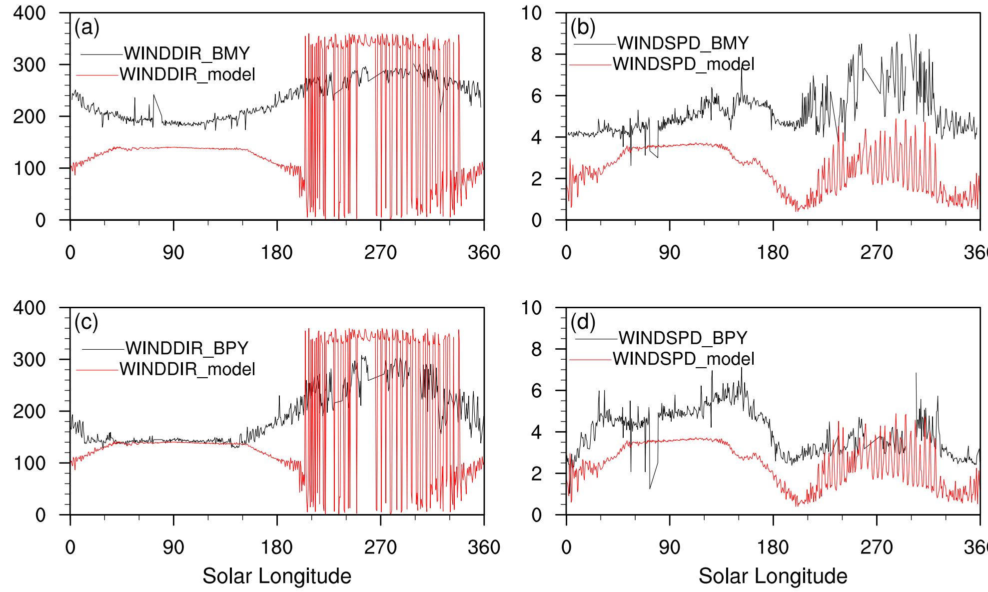

Figure 5. Comparisons of the (a and c) wind direction and (b and d) wind speed between the BMY and BPY measurements (the black lines) and the simulation results (the red lines). The top row (a and b) shows the BMY measurements and the bottom row (c and d) shows the BPY measurements. The units for wind direction and wind speed are degrees and m/s, respectively.

much as 40 W/m^2, while the maximum increase in LWD is 20 W/m^2 (Figure S7 in Supporting Information S1). Therefore, the effect of dust on surface energy is negative. Conversely, due to the delay of the dust storm under the "Late Dust" scenario, the amount of dust during the sublimation of the southern CO_2 ice cap is less than that in the "Standard" scenario, therefore, the effect of dust on surface energy is positive. The "Late Dust" scenario

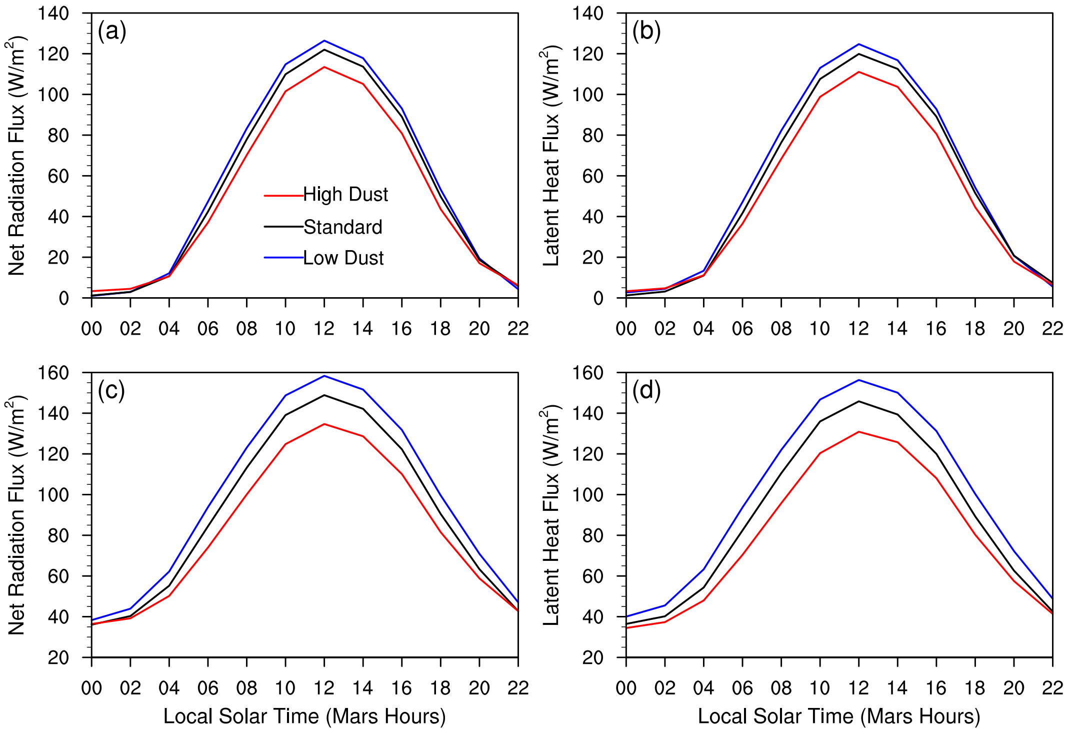

Figure 6. Diurnal variations in surface net radiation flux and latent heat flux averaged over southern CO_2 ice caps at (a and b) Ls = 210° and (c and d) Ls = 230°.

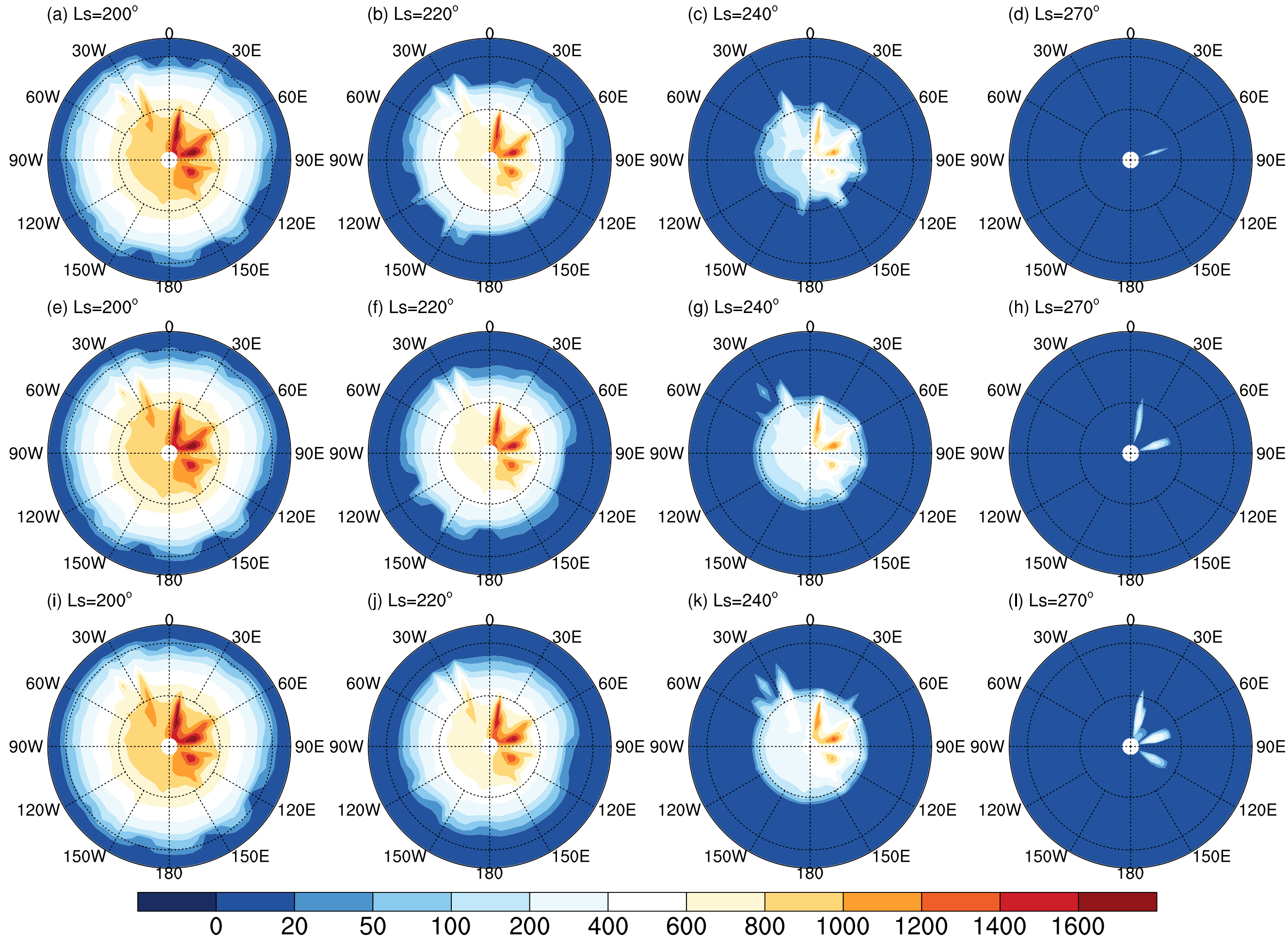

Figure 7. Spatial distribution of southern surface CO_2 ice (kg/m^2) in the (a–d) "Low Dust," (e–h) "Standard," and (i–l) "High Dust" scenarios during the sublimation of the southern ice cap. The outermost latitude is 55°S.

leads to an accelerated sublimation process (between Ls = 200 to Ls = 270), which is opposite to the phenomenon in the "Early Dust" scenario (Figure S8 in Supporting Information S1). Consequently, the negative effect of the "Late" dust storm (peaking at Ls = 280°) on the surface energy no longer matters since the southern ice cap is almost entirely sublimed away (Figures S8d and S8h in Supporting Information S1).

The deceleration in the sublimation of southern surface CO_2 ice in the "Early Dust" scenario can lead to a larger surface ice coverage area, that is, the ice edge can extend 5° more towards the equator relative to that under the "Standard" scenario. The change of ice edge under the "Late Dust" scenario, however, is not significant (Figure S9 in Supporting Information S1). For the northern CO_2 ice cap, its edge is hardly affected because the affected area of the surface ice cap is mainly limited to poleward of 80°N (Figure S10 in Supporting Information S1).

3.4. Impact of Dust Loading Strength on Atmospheric Circulation

Many studies have found that dust loading may affect Hadley circulation (Guzewich et al., 2016; Haberle et al., 1993; Wilson, 1997). Hadley circulation plays a key role in the interface structure formation of the easterlies and westerlies. However, current studies on the variation of typical wind belts are not comprehensive enough, especially in terms of the variation characteristics of near-surface wind fields, which are rarely considered. Figures 11a–11c depict the spatial distribution of the 1.5-m wind fields around the summer solstice in the Southern Hemisphere under the three dust loading scenarios. Three near-surface wind belts are significantly influenced by the dust loading. In the "High Dust" scenario, the westerlies near 30°S are strengthened, the easterlies near 10°N

10.1029/2021JE006937

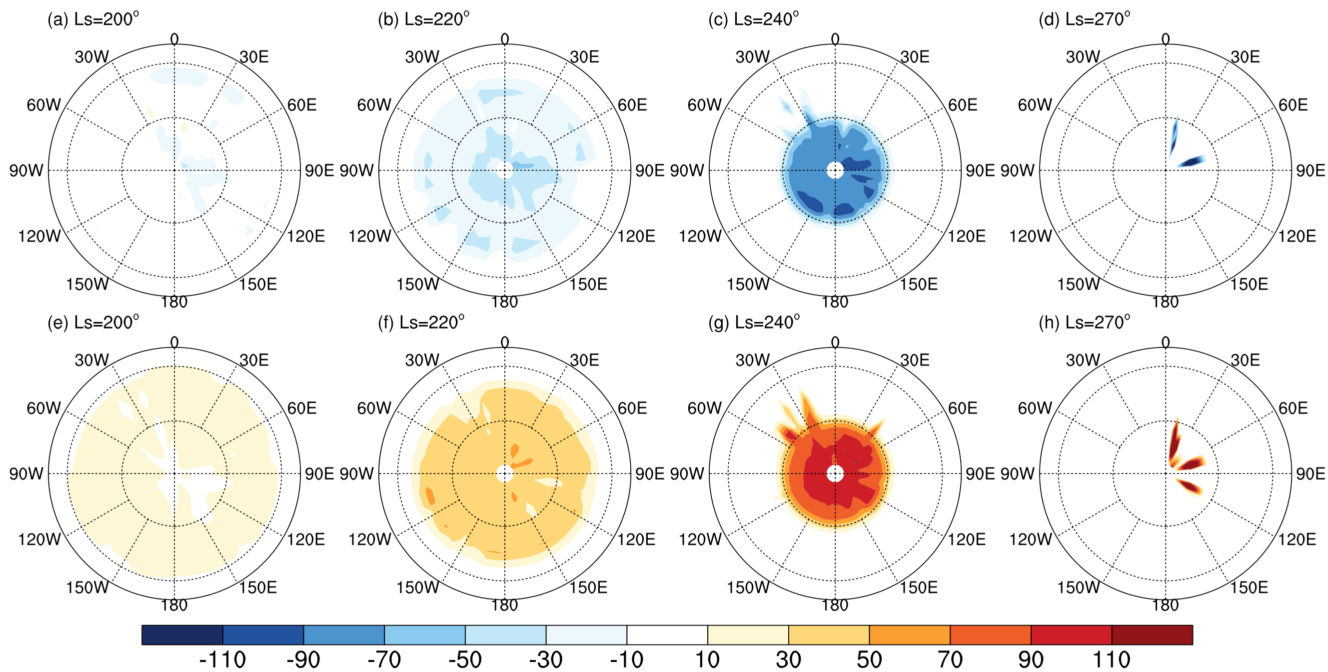

Figure 8. Southern surface CO_2 ice (kg/m^2) differences (a–d) between the "Low Dust" and "Standard" scenarios, and differences (e–h) between the "High Dust" and "Standard" scenarios during the sublimation of the southern ice cap. The outermost latitude is 55°S.

are weakened, and the westerlies in the northern polar region are weakened. It is worth noting that the strengthening of the westerlies near 30°S leads to increased suspended dust in the Hellas Basin (Figure 11f).

In the southern summer, airflow rises at the middle-to-low latitudes in the Southern Hemisphere (the ascending branch of the Hadley circulation) and sinks at the middle-to-low latitudes in the Northern Hemisphere (the sinking branch of the Hadley circulation) (Figure 12b). The strength of the vertical updrafts over the Southern Hemisphere increases with increasing dust loading (Figure 12c), leading to enhanced Coriolis acceleration on the returning flow near the surface (from north to south), which explains why the near-surface westerlies near 30°S strengthen. When the dust loading decreases, the downdraft over 0–20°N gets stronger (Figure 12a), which explains the increased near-surface wind speed around 10°N. In general, the entire meridional circulation expands and intensifies in the "High Dust" scenario compared with that in the "Standard" scenario, while the "Low Dust" scenario shows an opposite effect.

The enhanced updrafts in the "High Dust" scenario (Figure 12c) are affected by the Coriolis force, resulting in an increase in the upper easterly wind speed in the Southern Hemisphere. Furthermore, high dust loading can result in lower air temperature above the equator and higher air temperature above the northern polar region (Figures 3 and 4); specifically, the pole-to-equator temperature gradient increases, leading to easterly thermal winds over

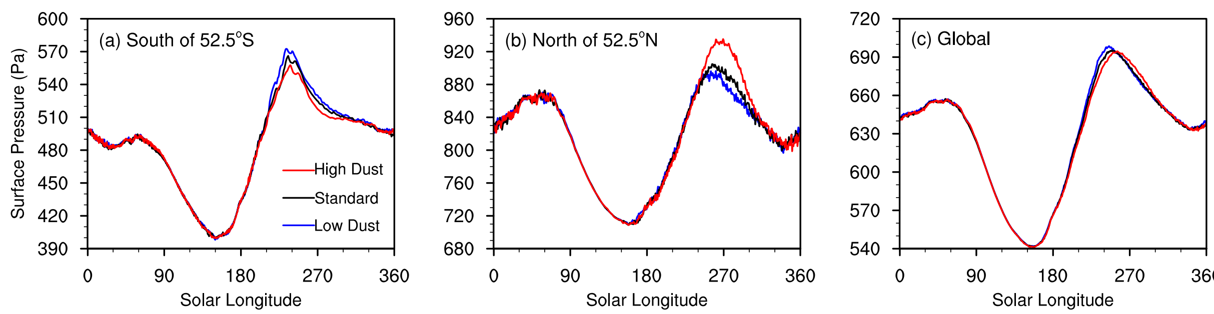

Figure 9. Temporal variations in surface pressure (in unit of Pa) averaged (a) south of 52.5°S and (b) north of 52.5°N and (c) across Mars under the three dust loading scenarios.

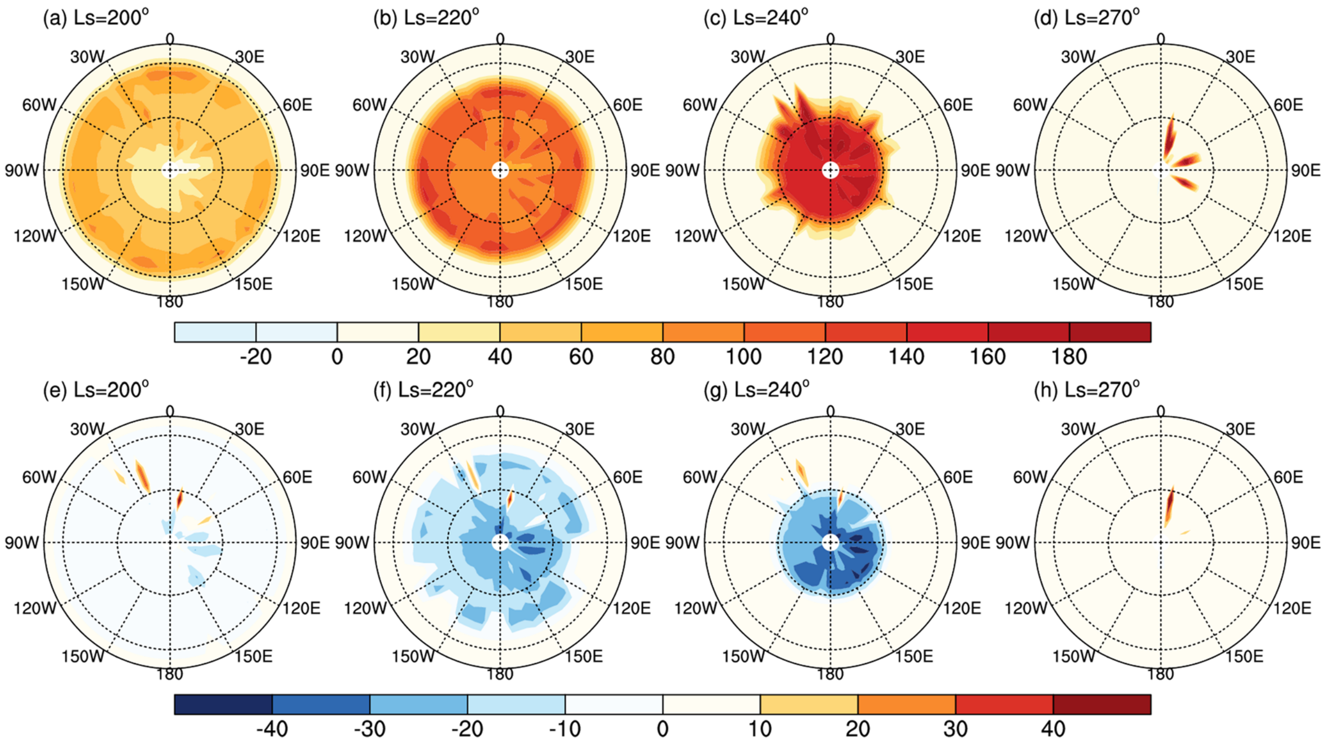

Figure 10. Southern surface CO_2 ice (kg/m^2) differences (a–d) between the "Early Dust" and "Standard" scenarios, and differences (e–h) between the "Late Dust" and "Standard" scenarios during the sublimation of the southern ice cap. The outermost latitude is 55°S.

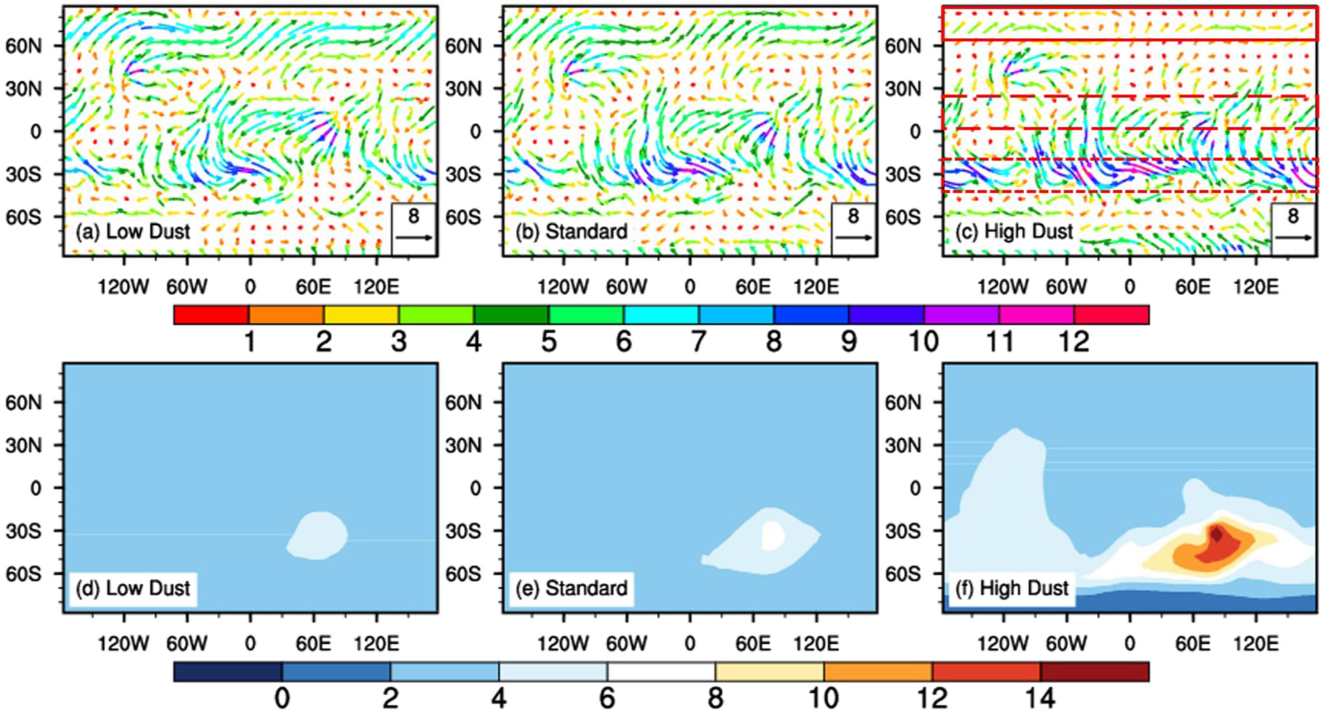

Figure 11. Spatial distribution of the daily mean wind fields at 1.5-m height (top row, units: m/s) and dust mixing ratio (bottom row, units: 10^{-5} kg/kg) in the "Low Dust" (first column), "Standard" (second column), and "High Dust" (third column) scenarios at Ls ≈ 270°. Red boxes denote three wind belts influenced by dust loading.

10.1029/2021JE006937

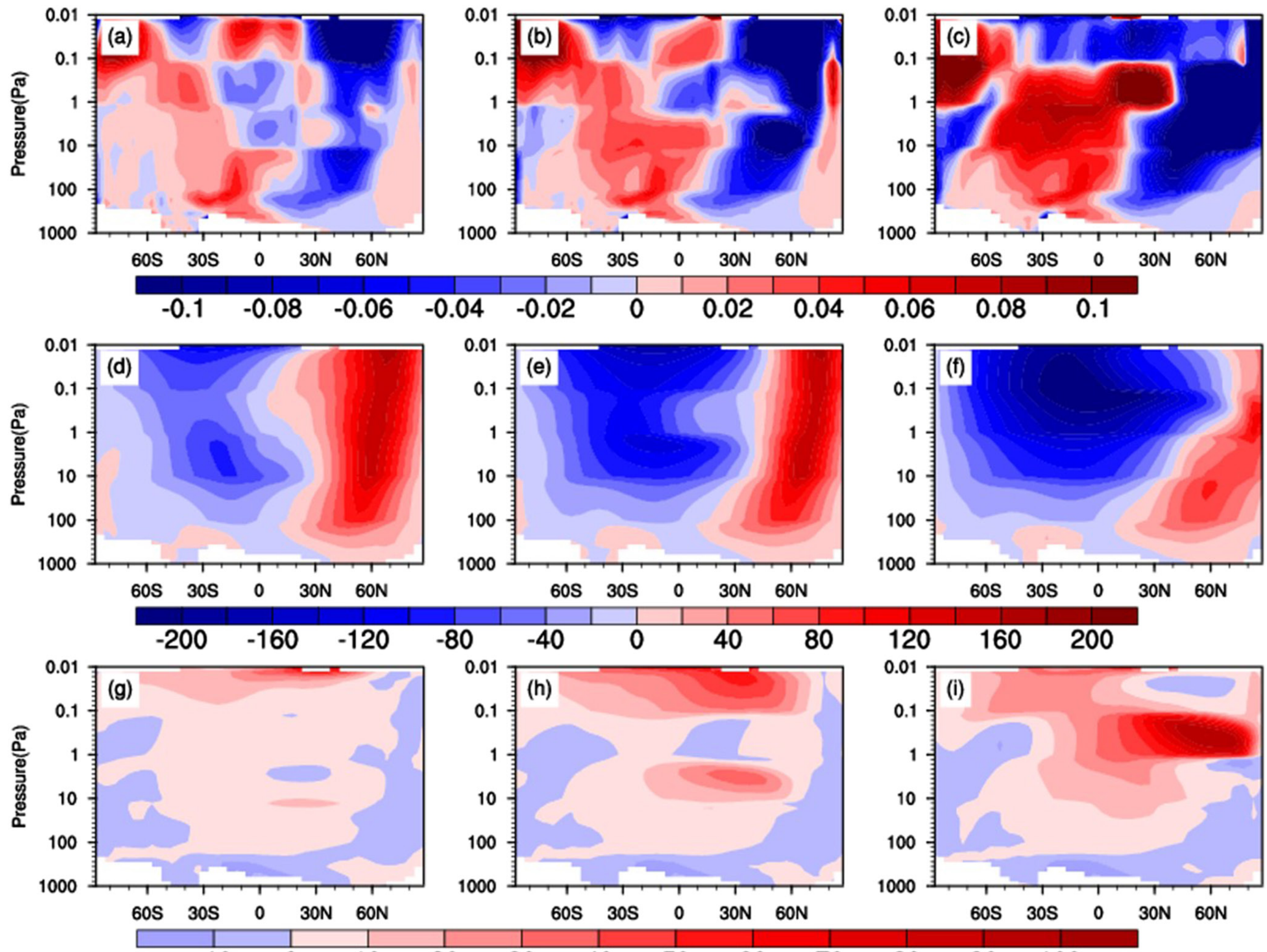

Figure 12. Latitude-pressure profiles of (a–c) vertical wind speed, (d–f) zonal wind speed, and (g–i) meridional wind speed in the "Low Dust" (first column), "Standard" (second column), and "High Dust" (third column) scenarios (units: m/s) at Ls ≈ 270°. Positive values represent updrafts, westerlies, and southerlies. Negative values represent downdrafts, easterlies, and northerlies.

the Northern Hemisphere according to the thermal wind balance. Therefore, the upper westerly winds over the northern middle latitudes under the “Standard” scenario turn into easterly winds under the "High Dust" scenario, and the easterlies even extend to high latitudes, leading to the weakening of the original upper westerlies over the northern polar region (Figure 12f), which may be related to the decrease in the near-surface westerly wind speed (Figure 11c).

The wind speed of the upper-air northerlies (the upper branch of the Hadley circulation) generally increases under higher dust loading, indicating that the meridional circulation from the summer hemisphere to the winter hemisphere is strengthened. The maximum variation in the meridional wind speed is mainly concentrated at 1–0.1 Pa in the Northern Hemisphere (Figure 12i).

3.5. Impact of Dust Loading Timing on Atmospheric Circulation

The analysis given in Section 3.2 shows that the warming vortex over the northern polar region induced by dust can impact the northern CO_2 ice cap. Figure 13 presents the temporal variations of air temperature over the Arctic at 5 Pa under the scenarios with different dust storm timings. It can be seen that the warming vortex in the “High Dust” (“Late Dust”) scenario appears around Ls = 250° (Ls = 280°), corresponding to the timing of dust loading peak. In the “Early Dust” scenario where the dust loading peak appears around Ls = 220°, the warming vortex

10.1029/2021JE006937

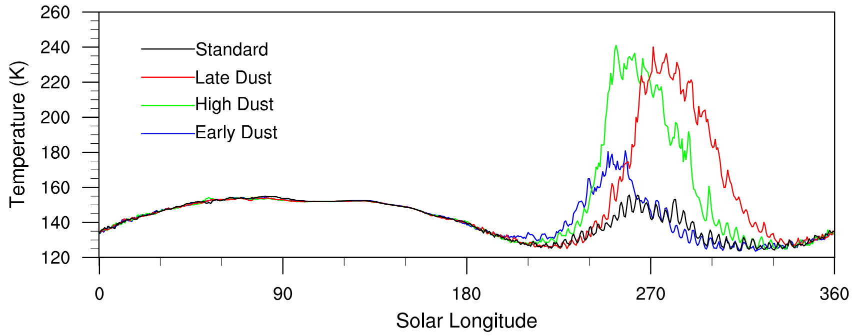

Figure 13. Temporal variations in air temperature at 5 Pa averaged over poleward of 80°N in the "Standard," "High Dust," "Early Dust," and "Late Dust" scenarios.

occurs at ~Ls = 250°, and its intensity is significantly weakened, that is, the maximum polar temperature is about 60 K lower than that of the "High Dust" and "Late Dust" scenarios.

The warming vortex is formed by the adiabatic warming associated with the downwelling branch of the Hadley circulation in the polar region (Guzewich et al., 2016). Figure 14 and Figure S11 in Supporting Information S1 show the latitude-pressure profiles of vertical and meridional wind speed changes under scenarios with different peak times of dust loading, respectively. It can be seen that in the "High Dust" and "Late Dust" scenarios, both the updrafts in the Southern Hemisphere (Figures 14e and 14i) and the upper meridional wind speed in the Northern

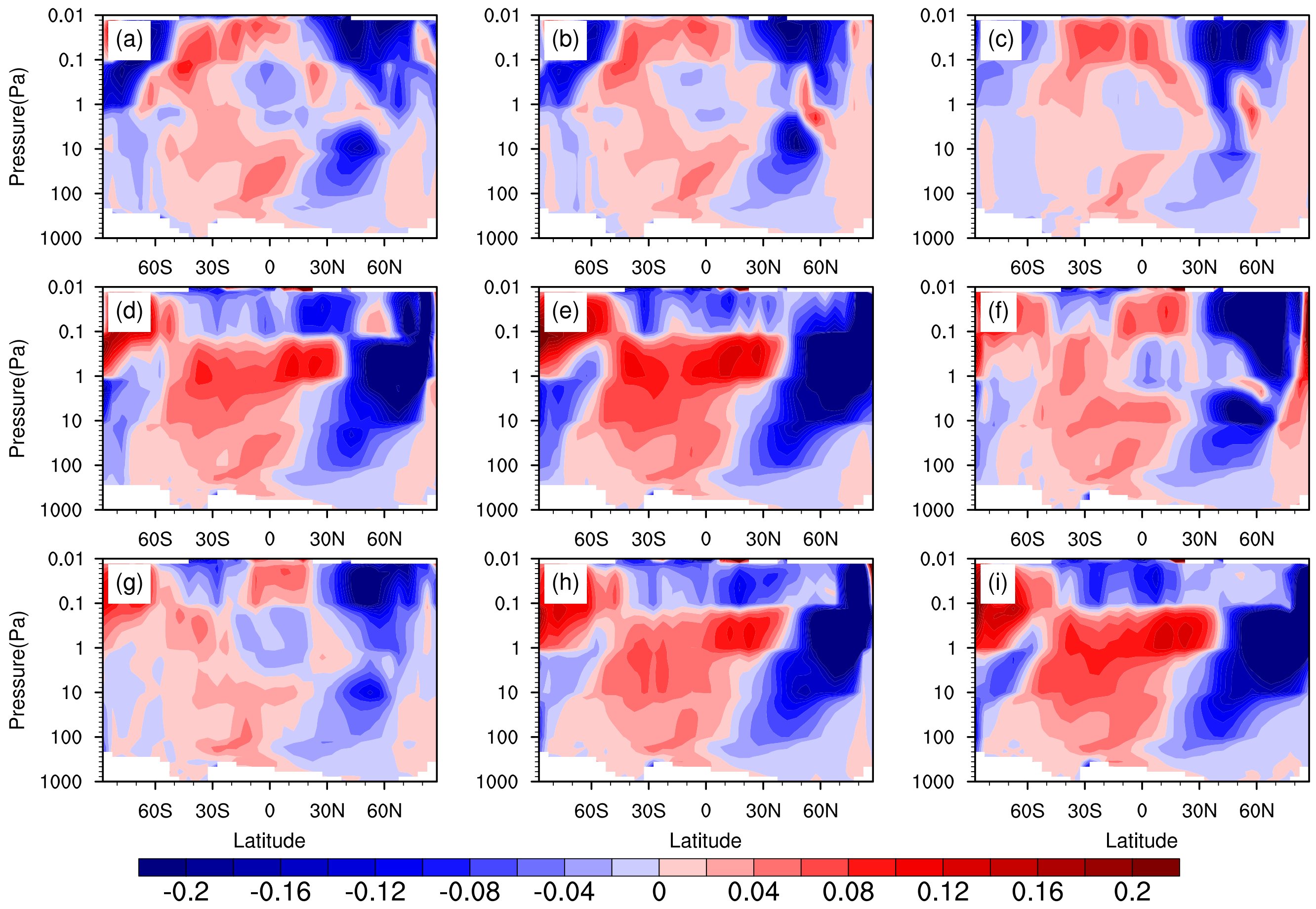

Figure 14. Latitude-pressure profiles of vertical wind speed changes (m/s) under the "Early Dust" (first column), "High Dust" (second column), and "Late Dust" (third column) scenarios at Ls ≈ 220° (first row), Ls ≈ 250° (second row), and Ls ≈ 280° (third row) compared with the "Standard" scenario.

10.1029/2021JE006937

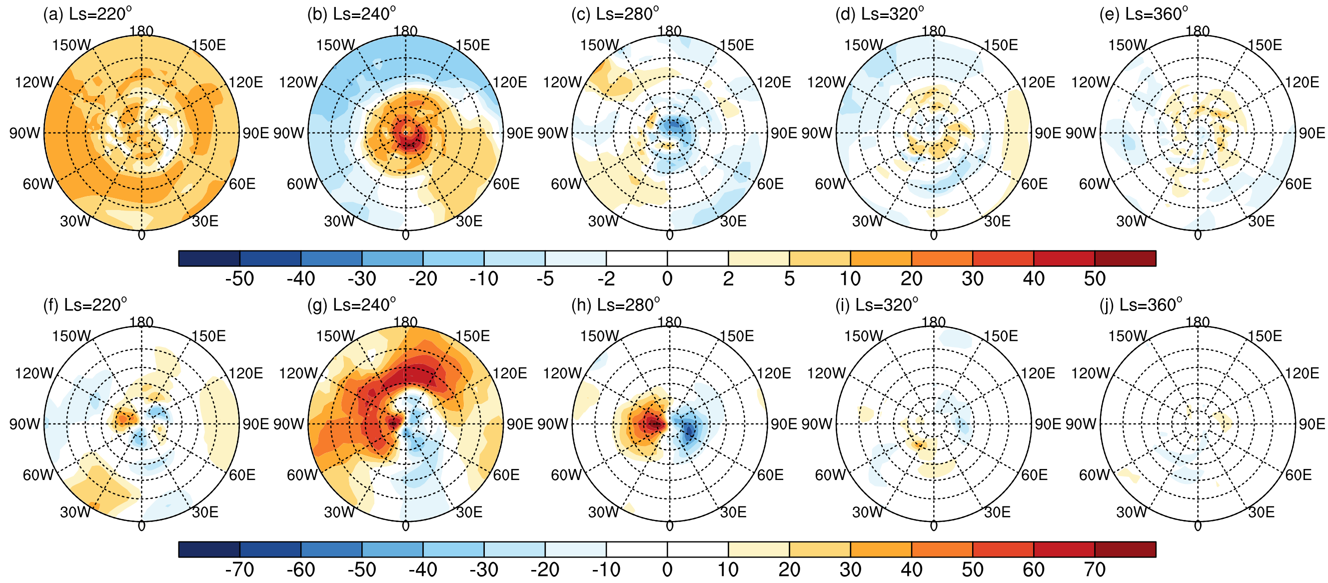

Figure 15. Differences in (a–e) air temperature (K) and (f–j) meridional wind speed (m/s) at 1 Pa between the "Early Dust" and "Standard" scenarios during the condensation of the northern ice cap. The outermost latitude is 0°.

Hemisphere (Figures S11e and S11i in Supporting Information S1) increase significantly when the dust loading reaches its peak value, which is also the time when northern warming vortex occurs. However, vertical and meridional wind speed in the "Early Dust" scenario change little when the peak dust loading occurs (Ls = 220°) (Figure 14a and Figure S11a in Supporting Information S1), which explains why we find no obvious warming over the northern polar region at this time. This may be related to the fact that the solar radiation in the southern hemisphere at Ls = 220° is not enough to drive the Hadley circulation. Subsequently, although the accumulated energy in the Southern Hemisphere increases (Figure 14d and Figure S11d in Supporting Information S1), the dust loading under the "Early Dust" scenario decreases, which eventually leads to weaker changes in the global-scale meridional circulation and the warming vortex. Besides, the decreased northern surface CO_2 ice mass in the "Early Dust" is less than that in other two scenarios due to the weakened warming vortex (Figure S12 in Supporting Information S1).

The warming over the northern polar region can inhibit the condensation process of CO_2, leading to decreased surface CO_2 ice mass, but why are there still areas with increased surface CO_2 ice in the Western Hemisphere (Figure S12 in Supporting Information S1)? There is little airborne dust in the northern high latitudes, so the radiative effect induced by dust is negligible. Under the "Early Dust" scenario, the atmosphere over the northern polar region became warmer around Ls = 240°, and the air temperature at low latitudes of the Northern Hemisphere decreases at the same time (Figure 15b). In addition, the enhancement of the meridional airflow in the Western Hemisphere transports upper cold air over the equator to the polar region (Figure 15g), accelerating the condensation process of gaseous CO_2, which explains the increase in surface CO_2 ice mass. Figure 16 shows the upper meridional wind speed and surface CO_2 ice mass in the polar region. The area in which the upper meridional wind speed increases corresponds to the area with increased surface CO_2 ice mass, and this phenomenon mainly occurs between Ls = 220° and Ls = 280°. There is little change of surface CO_2 ice mass after Ls = 280° (Figure 16). Similarly, the changes in the air temperature and meridional wind speed under the "High Dust" and "Late Dust" scenarios are also given in Figures S13-S16 in Supporting Information S1. In general, the above analyses indicate that the acceleration of the CO_2 condensation process in the Western Hemisphere is the result of the increased pole-to-equator temperature gradient and the increased meridional wind speed in the Western Hemisphere.

4. Conclusions and Discussion

Dust storms are a very common phenomenon on Mars. Five sensitivity experiments involving different magnitudes and timings of dust loading peak were designed to investigate the impacts of dust on Martian polar CO_2 ice caps and atmospheric circulation. The simulation results indicate that under the “Low (High) Dust” scenario,

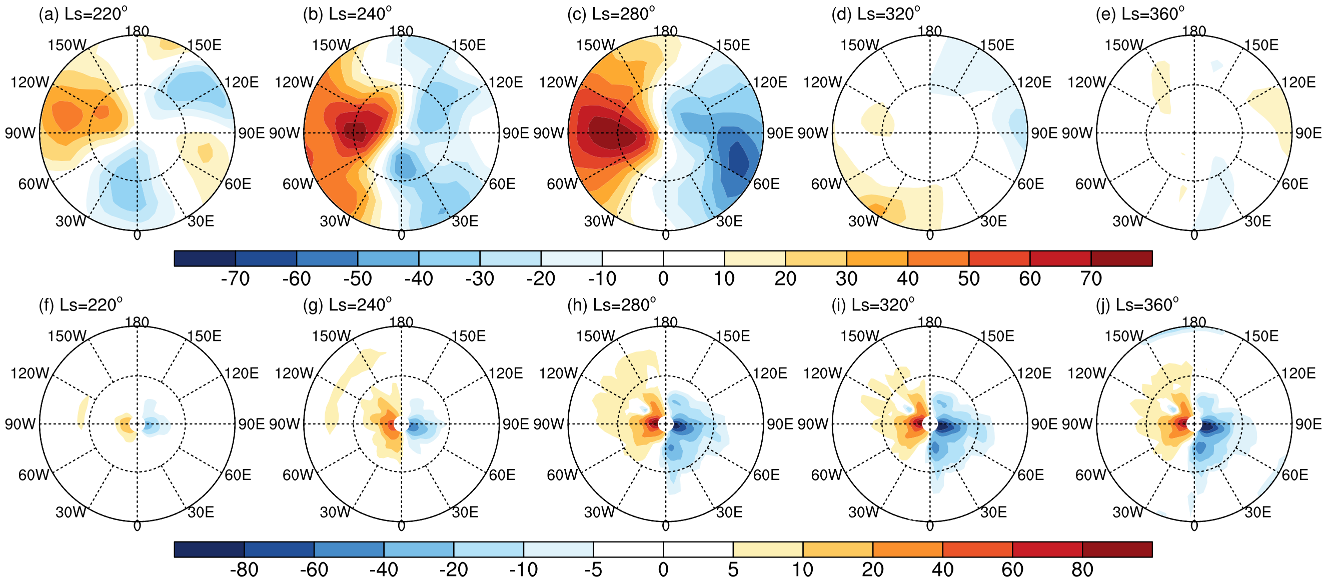

Figure 16. Differences in (a–e) meridional wind speed at 1 Pa (m/s) and (f–j) northern surface CO_2 ice (kg/m^2) between the "Early Dust" and "Standard" scenarios during the condensation of the northern ice cap. The outermost latitude is 60°N.

the southern surface ice cap retreats faster (slower). When Ls = 240°, the surface CO_2 ice mass under the "Low (High) Dust" scenario is 100 kg/m^2 less (more) than that in the "Standard" scenario. The ice edge under the "High Dust" scenario around Ls = 220° can extend up to 5° more equatorward than that under the "Standard" scenario. The coverage area of the northern CO_2 ice cap is hardly affected by the magnitude and timing of dust loading because the impact of warming vortex, which is induced by dust on the northern ice cap mainly appears north of 80°N. In terms of Martian dust storm timing, the dust storm under the "Early Dust" scenario inhibits the sublimation of the southern ice cap, while the dust storm under the "Late Dust" scenario can accelerate the sublimation process.

In addition, the variations in dust loading can lead to changes in three near-surface wind belts: specifically, in the "High Dust" scenario, the westerlies near 30°S are strengthened, the easterlies near 10°S are weakened, and the westerlies in the northern polar region are weakened. These phenomena are related to the strengthening of the ascending branch and the shift of the descending branch to the polar regions for global-scale meridional circulation. The appearance of the warming vortex over the northern polar region under the "Early Dust" scenario is delayed and its intensity is 60 K lower than that in the "High Dust" and "Late Dust" scenarios. The northern warming phenomenon can inhibit CO_2 condensation and reduce the surface CO_2 ice mass. However, there is increased northern surface CO_2 ice in the scenarios with more dust, which is the result of the increased temperature gradient of the Polar-Equator Direction and the increased meridional wind speed in the Western Hemisphere.

Piqueux et al. (2015) also analyzed the influence of Martian dust on the CO_2 cap extent in MY24–31 by defining the CO_2 ice cap as the regions in which diurnal radiometric temperature variations at ~32 μm wavelength do not exceed 5 K. They found that the dust storm in MY25 (similar to the "Early Dust" scenario in our study) has no significant effect on the northern CO_2 ice extent, but accelerates the recession of the southern CO_2 ice cap. The dust storm in MY28 (similar to the "Late Dust" scenario in our study) can result in the accelerated recession of the northern ice cap, and the southern CO_2 ice cap was not studied because the surface CO_2 ice almost entirely sublimated away when the dust storm occurred. The conclusions drawn by Piqueux et al. (2015) on the effects of the dust storm in MY25 are consistent with our analyses for the "Early Dust" scenario, but our results for the "Late Dust" scenario differ from those of the MY28 dust storm examined in their study. This difference may be related to the different criteria used to measure changes in the surface CO_2 ice cap (theirs is the area extent, and ours is the mass) and the different judgment for the periods of sublimation and condensation. In addition, the focus of our study is only on the impacts induced by airborne dust (that is, radiation effects and first-order changes in atmospheric circulation), whereas dust cover over the ice cap and dust redistribution due to changed atmospheric circulation are not taken into account.

Some limitations of this study remain. For example, the change in dust lifting and distribution due to the change in circulation is not considered and should be assessed in future work.

Data Availability Statement

The reconstructed observational data of column dust optical depth based on Montabone et al. (2015) are available at http://www-mars.lmd.jussieu.fr/mars/dust_climatology/index.html. The Mars Analysis Correction Data Assimilation (MACDA v1.0) (Montabone et al., 2014) is publicly available at http://data.ceda.ac.uk/badc/mgs/data/macda/v1-0. Mars Climate Sounder (MCS) observation data (McCleese et al., 2007) can be obtained from NASA's Planetary Data System (PDS): https://pds-atmospheres.nmsu.edu/data_and_services/atmospheres_data/MARS/mcs.html. Insight Lander observation data can be downloaded from Auxiliary Payload Sensor Suite (APSS) TWINS Bundle (Mora, 2019) with http://doi.org/10.17189/1518950. The data in generating the figures of the simulation results (Zhao et al., 2021) can be accessed at https://figshare.com/articles/dataset/MarsWRF_data/14370272.

Acknowledgments

The authors would like to acknowledge support received from the Frontiers Science Center for Planetary Exploration and Emerging Technologies of the University of Science and Technology of China. The authors also thank Editor Anni Määttänen and two anonymous reviewers for their constructive and helpful reviews, which greatly improved this manuscript.

References

Banfield, D., Rodriguez-Manfredi, J. A., Russell, C. T., Rowe, K. M., Leneman, D., Lai, H. R., et al. (2019). InSight Auxiliary Payload Sensor Suite (APSS). *Space Science Reviews*, *215*(1), 1–33. https://doi.org/10.1007/s11214-018-0570-x

Banfield, D., Spiga, A., Newman, C., Forget, F., Lemmon, M., Lorenz, R., et al. (2020). The atmosphere of Mars as observed by InSight. *Nature Geoscience*, *13*(3), 190–198. https://doi.org/10.1038/s41561-020-0534-0

Chow, K. C., Chan, K. L., & Xiao, J. (2018). Dust activity over the Hellas basin of Mars during the period of southern spring equinox. *Icarus*, *311*, 306–316. https://doi.org/10.1016/j.icarus.2018.04.011

Chow, K. C., Xiao, J., Chan, K. L., & Wong, C. F. (2019). Flow associated with the condensation and sublimation of polar ice caps on Mars. *Journal of Geophysical Research: Planets*, *124*, 1570–1580. https://doi.org/10.1029/2018je005848

Fonseca, R. M., Zorzano-Mier, M. P., & Martín-Torres, J. (2018). Planetary boundary layer and circulation dynamics at Gale Crater, Mars. *Icarus*, *302*, 537–559. https://doi.org/10.1016/j.icarus.2017.11.036

Forget, F., Hourdin, F., Fournier, R., Hourdin, C., Talagrand, O., Collins, M., et al. (1999). Improved general circulation models of the Martian atmosphere from the surface to above 80 km. *Journal of Geophysical Research*, *104*(E10), 24155–24175. https://doi.org/10.1029/1999je001025

Gebhardt, C., Abuelgasim, A., Fonseca, R. M., Martín-Torres, J., & Zorzano, M.-P. (2021). Characterizing dust-radiation feedback and refining the horizontal resolution of the MarsWRF model down to 0.5 degree. *Journal of Geophysical Research: Planets*, *126*, e2020JE006672. https://doi.org/10.1029/2020je006672

Guzewich, S. D., Toigo, A. D., & Waugh, D. W. (2016). The effect of dust on the Martian polar vortices. *Icarus*, *278*, 100–118. https://doi.org/10.1016/j.icarus.2016.06.009

Haberle, R., Pollack, J., Barnes, J., Zurek, R., Leovy, C., Murphy, J., et al. (1993). Mars atmospheric dynamics as simulated by the NASA Ames general circulation model. 1. The zonal-mean circulation. *Journal of Geophysical Research*, *98*(E2), 3093–3123. https://doi.org/10.1029/92je02946

Hong, S. Y., & Pan, H. L. (1996). Nonlocal boundary layer vertical diffusion in a Medium-Range Forecast Model. *Monthly Weather Review*, *124*(10), 2322–2339. https://doi.org/10.1175/1520-0493(1996)124<2322:nblvdi>2.0.co;2

Jiménez, P. A., Dudhia, J., González-Rouco, J. F., Navarro, J., Montávez, J. P., & García-Bustamante, E. (2012). A revised scheme for the WRF surface layer formulation. *Monthly Weather Review*, *140*(3), 898–918.

Kass, D. M., Schofield, J. T., Kleinböhl, A., McCleese, D. J., Heavens, N. G., Shirley, J. H., & Steele, L. J. (2019). Mars Climate Sounder observation of Mars' 2018 global dust storm. *Geophysical Research Letters*, *46*, e2019GL083931. https://doi.org/10.1029/2019GL083931

Kleinböhl, A., Schofield, J. T., Abdou, W. A., Irwin, P. G. J., & de Kok, R. J. (2011). A single-scattering approximation for infrared radiative transfer in limb geometry in the Martian atmosphere. *Journal of Quantitative Spectroscopy and Radiative Transfer*, *112*(10), 1568–1580.

Kleinböhl, A., Schofield, J. T., Kass, D. M., Abdou, W. A., Backus, C. R., Sen, B., et al. (2009). Mars Climate Sounder limb profile retrieval of atmospheric temperature, pressure, and dust and water ice opacity. *Journal of Geophysical Research*, *114*(E10), E10006. https://doi.org/10.1029/2009JE003358

Kuroda, T., Medvedev, A. S., Hartogh, P., & Takahashi, M. (2009). On forcing the winter polar warmings in the Martian middle atmosphere during dust storms. *Journal of the Meteorological Society of Japan*, *87*(5), 913–921. https://doi.org/10.2151/jmsj.87.913

McCleese, D. J., Schofield, J. T., Taylor, F. W., Calcutt, S. B., Foote, M. C., Kass, D. M., et al. (2007). Mars Climate Sounder: An investigation of thermal and water vapor structure, dust and condensate distributions in the atmosphere, and energy balance of the polar regions. *Journal of Geophysical Research*, *112*(E5), E05S06. https://doi.org/10.1029/2006je002790

Mischna, M. A., Lee, C., & Richardson, M. (2012). Development of a fast, accurate radiative transfer model for the Martian atmosphere, past and present. *Journal of Geophysical Research*, *117*(E10), E10009. https://doi.org/10.1029/2012je004110

Montabone, L., Forget, F., Millour, E., Wilson, R. J., Lewis, S. R., Cantor, B., et al. (2015). Eight-year climatology of dust optical depth on Mars. *Icarus*, *251*, 65–95. https://doi.org/10.1016/j.icarus.2014.12.034

Montabone, L., Marsh, K., Lewis, S. R., Read, P. L., Smith, M. D., Holmes, J., et al. (2014). The Mars Analysis Correction Data Assimilation (MACDA) dataset V1.0. *Geoscience Data Journal*, *1*(2), 129–139. https://doi.org/10.1002/gdj3.13

Montmessin, F., Forget, F., Rannou, P., Cabane, M., & Haberle, RM. (2004). Origin and role of water ice clouds in the Martian water cycle as inferred from a general circulation model. *Journal of Geophysical Research*, *109*, E10004. https://doi.org/10.1029/2004je002284

Mora, L. (2019). APSS TWINS data. *Atmospheres Node*. https://doi.org/10.17189/1518950

Newman, C. E., Kahanpää, H., Richardson, M. I., Martínez, G. M., Vicente-Retortillo, A., & Lemmon, M. T. (2019). MarsWRF convective vortex and dust devil predictions for Gale crater over 3 Mars years and comparison with MSL-REMS observations. *Journal of Geophysical Research: Planets*, *124*(12), 3442–3468. https://doi.org/10.1029/2019je006082

Newman, C. E., Lee, C., Mischnac, M. A., Richardsona, M. I., & Shirleyc, J. H. (2019). An initial assessment of the impact of postulated orbit-spin coupling on Mars dust storm variability in fully interactive dust simulations. *Icarus*, *317*, 649–668. https://doi.org/10.1016/j.icarus.2018.07.023

Newman, C. E., & Richardson, M. I. (2015). The impact of surface dust source exhaustion on the Martian dust cycle, dust storms and interannual variability, as simulated by the MarsWRF General Circulation Model. *Icarus*, *257*, 47–87. https://doi.org/10.1016/j.icarus.2015.03.030

Piqueux, S., Kleinböhl, A., Hayne, P. O., Kass, D. M., Schofield, J. T., & McCleese, D. J. (2015). Variability of the Martian seasonal CO_2 cap extent over eight Mars Years. *Icarus*, *251*, 164–180. https://doi.org/10.1016/j.icarus.2014.10.045

Rafkin, S. C. R., Hollingsworth, J. L., Mischna, M. A., Newman, C. E., & Richardson, M. I. (2013). Mars: Atmosphere and climate overview. In *Comparative climatology of terrestrial planets*. https://doi.org/10.2458/azu_uapress_9780816530595-ch003

Richardson, M. I., Toigo, A. D., & Newman, C. E. (2007). PlanetWRF: A general purpose, local to global numerical model for planetary atmospheric and climate dynamics. *Journal of Geophysical Research*, *112*(E9), 29. https://doi.org/10.1029/2006je002825

Senel, C. B., Temel, O., Lee, C., Newman, C. E., Mischna, M. A., Muñoz-Esparza, D., et al. (2021). Interannual, seasonal and regional variations in the Martian convective boundary layer derived from GCM simulations with a semi-interactive dust transport model. *Journal of Geophysical Research: Planets*, *126*, e2021JE006965. https://doi.org/10.1029/2021je006965

Skamarock, W. C., & Klemp, J. B. (2008). A time-split nonhydrostatic atmospheric model for weather research and forecasting applications. *Journal of Computational Physics*, *227*(7), 3465–3485. https://doi.org/10.1016/j.jcp.2007.01.037

Spiga, A., Banfield, D., Teanby, N. A., Forget, F., Lucas, A., Kenda, B., et al. (2018). Atmospheric science with InSight. *Space Science Reviews*, *214*(7). https://doi.org/10.1007/s11214-018-0543-0

Toigo, A. D., Lee, C., Newman, C. E., & Richardson, M. I. (2012). The impact of resolution on the dynamics of the Martian global atmosphere: Varying resolution studies with the MarsWRF GCM. *Icarus*, *221*(1), 276–288. https://doi.org/10.1016/j.icarus.2012.07.020

Towner, M. C. (2009). Characteristics of large Martian dust devils using Mars Odyssey thermal emission imaging system visual and infrared images. *Journal of Geophysical Research*, *114*, E02010. https://doi.org/10.1029/2008je003220

Whelley, P. L., & Greeley, R. (2008). The distribution of dust devil activity on Mars. *Journal of Geophysical Research*, *113*(E7), E07002. https://doi.org/10.1029/2007je002966

Wilson, R. J. (1997). A general circulation model simulation of the Martian polar warming. *Geophysical Research Letters*, *24*(2), 123–126. https://doi.org/10.1029/96gl03814

Wu, Z., Richardson, M. I., Zhang, X., Cui, J., Heavens, N. G., Lee, C., et al. (2021). Large eddy simulations of the dusty Martian convective boundary layer with MarsWRF. *Journal of Geophysical Research: Planets*, *126*, e2020JE006752. https://doi.org/10.1029/2020je006752

Xiao, J., Chow, K.-C., & Chan, K.-l. (2019). Dynamical processes of dust lifting in the northern mid-latitude region of Mars during the dust storm season. *Icarus*, *317*, 94–103. https://doi.org/10.1016/j.icarus.2018.07.020

Zhao, Y., Zhong, L., Yuan, R., Zhao, C., Li, R., Wang, Y., et al. (2021). MarsWRF_data. Figshare. Dataset. Retrieved from https://figshare.com/articles/dataset/MarsWRF_data/14370272